Mapping Impervious Surface Distribution and Dynamics in an Arid/Semiarid Area-A Case Study in Ordos, China

WEI GUO[1], CHUANWU ZHAO[1], YUHUAN ZHANG[2], AND SHANGQING GAO[3]

[1]College of Geoscience and Surveying Engineering, China University of Mining and Technology, Beijing 100083, China
[2]Satellite Environment Center, Ministry of Environmental Protection, Beijing 100094, China
[3]Graduate School of Education, Beijing Foreign Studies University, Beijing 100089, China

Corresponding author: Chuanwu Zhao (cumtb_zhao@163.com)

ABSTRACT The impervious surface area (ISA) has become an important parameter in the areas such as surface runoff, climate change, and socioeconomic analysis. However, using remote sensing data to accurately map ISA is still difficult due to its complexity in the arid and semi-arid areas with large amounts of bare soil, sparse vegetation, and a small ISA. In this study, we have selected Ordos city as study area and examined the spatial pattern and dynamics in the years of 1990, 1995, 2000, 2005, 2010, 2015, and 2019 by using multiple data sources with a combination method. The results indicate that the ISAs in 2010, 2015, and 2019 were extracted with overall accuracies of 90.6%, 89.2%, and 91.8% with kappa coefficients of 0.79, 0.76, and 0.82, respectively. The ISA extraction results of the Urban Index (UI), Normalized Difference Built-Up Index (NDBI), Index-based Built-Up Index (IBI), and Impervious Built-up Index from optical sensors (IBUIopt) were used for comparison. Meanwhile, a correlation analysis between socioeconomic factors and the ISA of the typical resource-based city of Ordos was conducted. The spatial pattern and dynamics of the ISA data in Ordos city are of great significance to the study of socioeconomic and environmental changes and provide a reference to examine the effect of ISAs in other resource-based cities.

INDEX TERMS Impervious surface area, Landsat, VIIRS-DNB, nighttime light.

I. INTRODUCTION

With the rapid development of global urbanization, over half of the World's population (54%) lives in urban areas [1]. The urban population in the world will reach 6.3 billion and the ratio is projected to 66% of the world's population by 2050 [2]. Urbanization is not only related to population growth but also the economic development [3], [4]. There are many kinds of research that have demonstrated that the city development model can affect the economic development and ecological environment [5], [6]. Impervious surfaces are usually defined as man-made features that do not allow water to penetrate through the ground, e.g., cement roads, building roofs, and parking lots. Impervious surface area (ISA)

The associate editor coordinating the review of this manuscript and approving it for publication was Inês Domingues.

is not only an indicator of urban development, but also a key sensitive parameter to monitor environmental quality in built-up areas [7]. Hence, mapping the ISA in urban areas is important because it is beneficial to the sustainable city development.

The arid/semiarid areas cover a large area of the earth's land surface, are especially vulnerable as low precipitation and ISA increases. Moreover, these cities tend to have a high population concentration [8]–[11], where the rapid development of the economy has accelerated the process of urbanization and made urban areas expand outward that resulted in increasing ISA size [12]–[14]. This has a series of impacts on the ecological environment, such as vegetation degradation, increased water pollution, and increased energy consumption [15]–[20]. Therefore, the timely and accurate understanding of the current situation of urban development

and its dynamics in arid/semiarid regions is of great significance.

Due to the limitations of traditional surveying techniques, remote sensing imagery has been widely used in recent years, having several advantages such as wide coverage, fast information acquisition, and spatial consistency [21], [22]. Multiple remote-sensing data sources have been used in ISA mapping, such as high (from the Ikonos-2, Gaofen-1, and QuickBird satellites), medium (from the Landsat program), and coarse spatial resolution images (e.g., Moderate Resolution Imaging Spectroradiometer (MODIS) and nighttime light (NTL) data) [15], [21], [23]. High spatial resolution images can achieve better results when used for fine classification [24], ISA mapping [25]–[27] and urban building extraction [28], [29]. However, the data acquisition from these sources comes at a high cost, more time-consumption and laborious, that makes long-term sequence monitoring not easily performed [30]. Medium and coarse spatial resolution images are the most commonly used data sources because of their easy accessibility and long-time horizon. The spectral index method based on a single remote sensing data source is widely used such as, the Urban Index (UI) [31], Normalized Difference Built-Up Index (NDBI) [32], Index-based Built-Up Index (IBI) [33], Impervious Built-up Index from optical sensors (IBUIopt) [34]. However, due to the complex spectral properties of the features, classification and extraction cannot be effectively performed using a single remote sensing data source. Nevertheless, the development of NTL imagery (e.g., Defense Meteorological Satellite Program Operational Linescan System (DMSP-OLS) and Visible Infrared Imaging Radiometer Suite with Day/Night Band (VIIRS-DNB)) has solved the above problems.

NTL remote sensing records areas with dense human socioeconomic activity, such as cities, towns, and factories, on the surface of the earth [35]–[37]. NTL data show a negative correlation with human activities such as poverty, while a positive correlation with energy consumption, urban extent, and gross domestic product (GDP) [38]–[42]. Several kinds of research on ISA extraction have been implemented by employing NTL remote sensing imagery. Bagan et al. used DMSP-OLS data to map ISA distribution at the global scale [43]. Lawrence et al. and Zhou et al. used the thresholding approach of the NTL data to map large scale ISA spatial distribution [44], [45]. Due to the blooming effects and coarse spatial resolution in the NTL data, only using NTL data to map ISA will inaccurate [21], [22]. Lu et al. [46] estimated the fractional ISA in southeast China based on the combination of DMSP OLS and MODIS NDVI (normalized difference vegetation index) data with high accuracy. Therefore, a lot of studies have shifted towards combination of multiple remote sensing data sources [15], [47], [48]. Guo et al. proposed a framework based on the combination of DMSP-OLS and MODIS NDVI data to estimate impervious areas [47]. Guo et al. developed the modified impervious surface index (MISI) based on the VIIRS DNB and Provb-V data to map ISA distribution in China [15]. This combination has been proven effective in increasing ISA mapping accuracy in urban landscapes. Xue et al. used VIIRS nighttime light data and Landsat 8 multispectral data to delineate urban boundaries with high accuracy [48]. A combination method based on multiple data sources has proven effective in improving ISA mapping accuracy in complex urban landscapes [15]. However, this method is rarely used in arid/semi-arid areas, and the potential of this method has not been explored in the face of the similarity between ISA spectral characteristics and bare soil with medium and high spatial resolution images [10].

The reviewed literature on spectral indices leads us to conclude that these indices have not been comprehensively addressed the confusion between impervious surface and bare soil. Moreover, it has been shown that nighttime light data has great potential for impervious surface extraction. Therefore, this study aims to develop an effective framework to map the accurate ISA distribution for arid/semiarid areas derived from three Landsat sensors (TM, ETM+, OLI-TIRS) and two NTL sensors (DMSP-OLS, VIIRS-DNB). Ordos city in China is selected for this research and the spatial pattern and dynamics were examined in 1990, 1995, 2000, 2005, 2010, 2015, and 2019. The ISA mapping results obtained using the framework in this paper were compared with the results of other remote sensing indices (UI, NDBI, IBI, and IBUIopt). The relationship between socioeconomic factors and the ISA is also conducted. The results of this study provide a framework for mapping impervious surface areas in arid/semiarid areas.

II. STUDY AREA AND DATASETS
A. STUDY AREA
Ordos is a typical resource-based city located in semi-arid area [49], [50]. It is selected as the study area for this research, that includes two experiments. First experiment demonstrates to the accurate extraction of ISA from 30 m spatial resolution images to analyze the ISA spatial patterns and examine the ISA dynamics in Ordos over the 30 years from 1990 to 2019. Secondly, this research aims to explore the potential relationship between the ISA of a typical resource-based city (Ordos) and its socioeconomic circumstances via correlation analysis. Ordos is a prefecture-level city located in the southwest of the Inner Mongolia Autonomous Region (Figure 1), which is around 340 km in the north-south, 400 km in the east-west direction. It has an area of 86,900 km^2 and elevation between 792 m and 1777 m. Its terrain is low in the northeast and high in the southwest. The hilly and gully areas in the east and the wavy plateau areas in the west covers around 30% and 24% of the total land area, respectively. Moreover, the Kubuqi desert and Maowusu sandy land in the middle and the Yellow River area in the north account for around 40% and 6% of the total land area respectively [51]. Ordos has a temperate continental climate with an average annual temperature between 6.7-8.4 °C, an annual sunshine duration between 2881-3221.6 h, average annual relative humidity between 43-49%, average annual precipitation between 252-670 mm, and annual evaporation ranging from 2000-3000 mm [52].
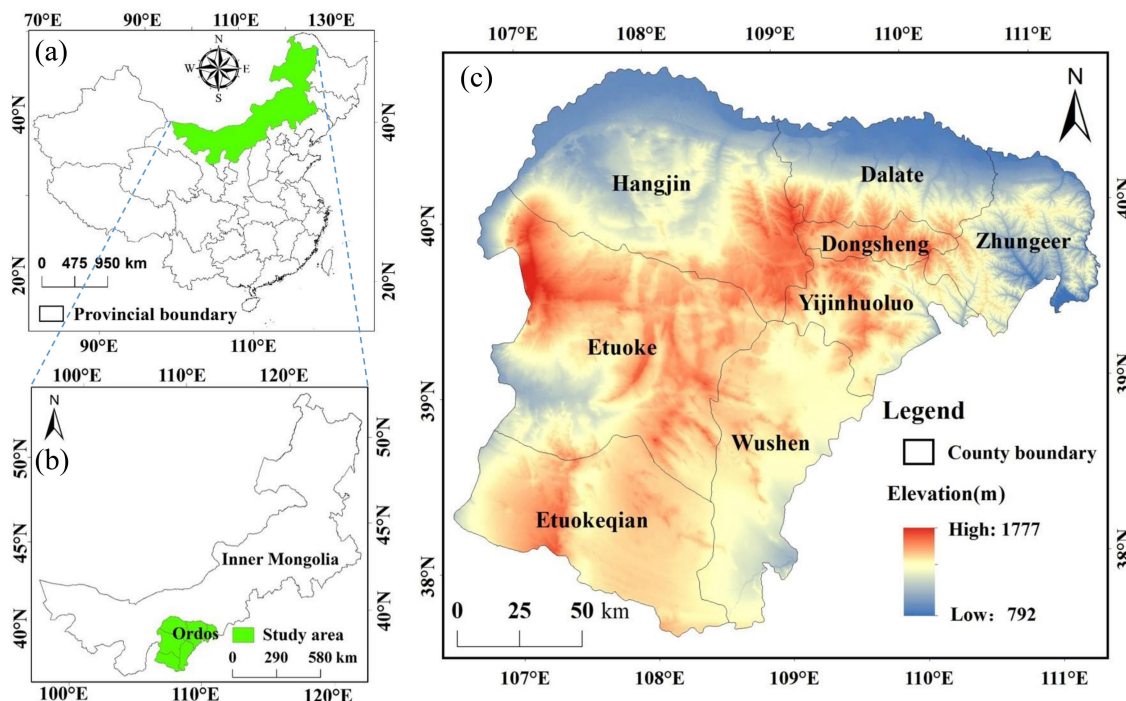
FIGURE 1. The study area location: (a) Inner Mongolia in northern China, (b) Ordos in the southwest of Inner Mongolia, and (c) a detailed map of Ordos.

B. DATASETS

The datasets employed in this study are shown in the Table 1, including NTL (DMSP-OLS in 1990, 1995, 2000, 2005 and 2010, and VIIRS-DNB in 2015 and 2019), Landsat multi-spectral data (Landsat-TM (Thematic Mapper) in 1990, 1995, 2000, and 2010, Landsat-ETM+ (Enhanced TM) in 2005, and Landsat-OLI (Operational Land Imager) in 2015 and 2019), and high-spatial resolution imagery from Google Earth are used to collect validation samples.

In addition to the remote sensing data, the socioeconomic data (http://tj.nmg.gov.cn/ndsj/index.html) are also selected. These datasets include: National Economy (i.e., total GDP (TGDP), GDP in secondary industry (GDPS), GDP in tertiary industry (GDPT), per-capita GDP (PGDP)), Population (i.e., registered population (RGP), resident population (RSP), urban population (UP), rural population (RP)), Income (i.e., local government revenue (LGR), resident saving deposits (RSD), per-capita net income of peasants and herdsmen (PNI), per-capita disposable income of urban residents (PDI)), Product and Investment (i.e., coal production (CP), investment in fixed assets (IFA), power generation (PG)).

III. METHODS

The framework of mapping the ISA distribution using multi-source remotely sensed data is shown in Figure 2. There are three major steps: (1) extraction of the initial ISA data from the NTL data for the selected city, (2) refinement of the initial ISA to make detailed ISA distribution using Landsat images through the removal of non-ISA areas, and (3) accuracy

analysis of the ISA estimation and examination of the ISA spatial patterns and dynamics from 1990–2019.

A. EXTRACTION OF THE INITIAL ISA DATA FROM THE NTL DATA

1) PREPROCESSING OF THE NTL DATA

Both the VIIRS-DNB and DMSP-OLS with geographic systems re-projected into the ACEA coordinate system in order to make the demonstration more convenient. The time-series VIIRS-DNB data was resampled with nearest-neighbor resampling algorithm to a cell size of 500×500 m and the time-series DMSP-OLS data to a cell size of 1×1 km.

Since the DMSP-OLS NTL images are not calibrated for on-orbit radiation, they cannot be directly used for research. In this study, the DMSP-OLS data was corrected using the invariant region method [53]. Jixi city, Heilongjiang was selected as the invariant region area, and the NTL data of Jixi city taken by F16 satellites in 2005 was used as the frame of reference [54]. The formula to establish the calibration model expressed as (1):

$$DN\_correct_i = C_0 \times DN_i^2 + C_1 \times DN_i + C_2 \qquad (1)$$

where DN_i and $DN\_correct_i$ are the digital number values of the ith pixel before and after correction while C_0, C_1, and C_2 are the regression coefficient constant terms for the quadratic polynomial. The parameter values of the quadratic polynomial regression correction model of the image to be corrected and the reference image are reported in the Table 2. Using the corresponding quadratic polynomial model equations, each

TABLE 1. The multitemporal and high spatial resolution datasets.

Data	Acquisition time	Data description	Data source
DMSP-OLS	1992 1995 2000 2005 2010	The Version 4 DMSP-OLS data under WGS84 spatial reference system in 1992, 1995, 2000, 2005, and 2010 were downloaded. These data were reprojected to Albers Conical Equal Area (ACEA) projection with cell size of 1 km by 1 km.	National Geophysical Data Center (http://ngdc.noaa.gov/eog/dmsp/downloadV4composites.html)
VIIRS-DNB	2015 March-April 2019	The 2015 annual data were downloaded. The 2019 VIIRS DNB data in months of March-April were downloaded. The mean DNB image based on the two-month data were used to represent the yearly DNB with 500 spatial resolutions to reduce the impact of outliers and non-ISA points (e.g., fires, ships) on ISA mapping. The 2015-2019 VIIRS DNB images were reprojected to ACEA projection with cell size of 500 m by 500 m.	National Centers for Environmental Information (NCEI) (https://ngdc.noaa.gov/eog/viirs/download_dnb_composites.html)
Landsat TM, ETM+, and OLI	May-October 1990-2019. 63 scenes, including: 126/032-126/033 127/032-127/033 128/032-128/034 129/032-129/033 (Appendix A)	For each year, 9 scenes of Landsat images (L5 TM in 1990, 1995, 2000 and 2010, L7 ETM+ in 2005, and L8 OLI in 2015 and 2019) without clouds or less than 1% of clouds, which were acquired in growing season, were used. All these images with L1T product were downloaded and used for mapping of impervious surface distribution at 30 m spatial resolution.	United States Geological Survey (http://earthexplorer.usgs.gov/)
High-resolution images	2010 2015 2019	High spatial resolution images from the Google Earth were used for collection of validation samples in 2010, 2015, and 2019.	Google Earth website (https://www.google.com/earth)
Vector data	2017	Chinese administrative boundaries were obtained at the scale of 1:1,000,000	National Geomatics Center of China (NGCC) (http://www.ngcc.cn/ngcc/)

TABLE 2. Parameters of the quadratic polynomial regression model.

Satellite	Year	C_0	C_1	C_2	R^2
F10	1992	-0.0036	1.5413	-0.8426	0.9511
F12	1995	-0.0063	1.0426	-1.1415	0.9121
F14	2000	-0.0054	1.3409	1.0842	0.9105
F15	2000	-0.0002	1.0472	0.1325	0.9647
	2005	-0.0039	1.3812	0.7123	0.9216
F16	2005	-0.0057	1.3869	-0.0026	0.9732
F18	2010	-0.0086	0.1463	1.5257	0.9225

Note: R^2 is the coefficient of determination for the fitted model.

DMSP-OLS night light image that is required to be corrected in the study area.

In addition, we used the annual correction model proposed by Liu *et al.* to make full use of the night light information obtained by different satellites in the same year [55]. The model can be expressed as (2):

$$DN_i = \begin{cases} 0, & DN_i^a = 0 \ or \ DN_i^b = 0 \\ \left(DN_i^a + DN_i^b\right)/2, & otherwise \end{cases} \quad (2)$$

where DN_i^a and DN_i^b are the digital number values of the ith pixel obtained by two different satellites after mutual

correction, and DN_i represents the digital number value of the ith pixel after correction.

2) THE NORMALIZED NTL DATA

The majority of the VIIRS-DNB data values were less than 70 nWcm^{-2}sr^{-1}, so we set 70 as the maximum threshold for this data source in this research, in other words, pixel values that are more than 70 were assigned as 70 [49]. Meanwhile, the DMSP-OLS data have a small range of 0–63. The VIIRS-DNB data and DMSP-OLS data is normalized as (3):

$$NTL_{nor} = \frac{NTL - NTL_{min}}{NTL_{max} - NTL_{min}} \quad (3)$$

where NTL_{nor} is the normalized DMSP-OLS (VIIRS-DNB) image while NTL_{max} and NTL_{min} represent the maximum and minimum values in the VIIRS-DNB imagery and DMSP-OLS imagery respectively. In addition, it should be noted that we have adopted the method of [22] as the VIIRS-DNB data processing method for March–April 2019.

For the VIIRS-DNB imagery, we used the *IISI* to get the initial ISA which can improve ISA mapping performance in arid/semiarid regions [10]. The *IISI* can be calculated using (4):
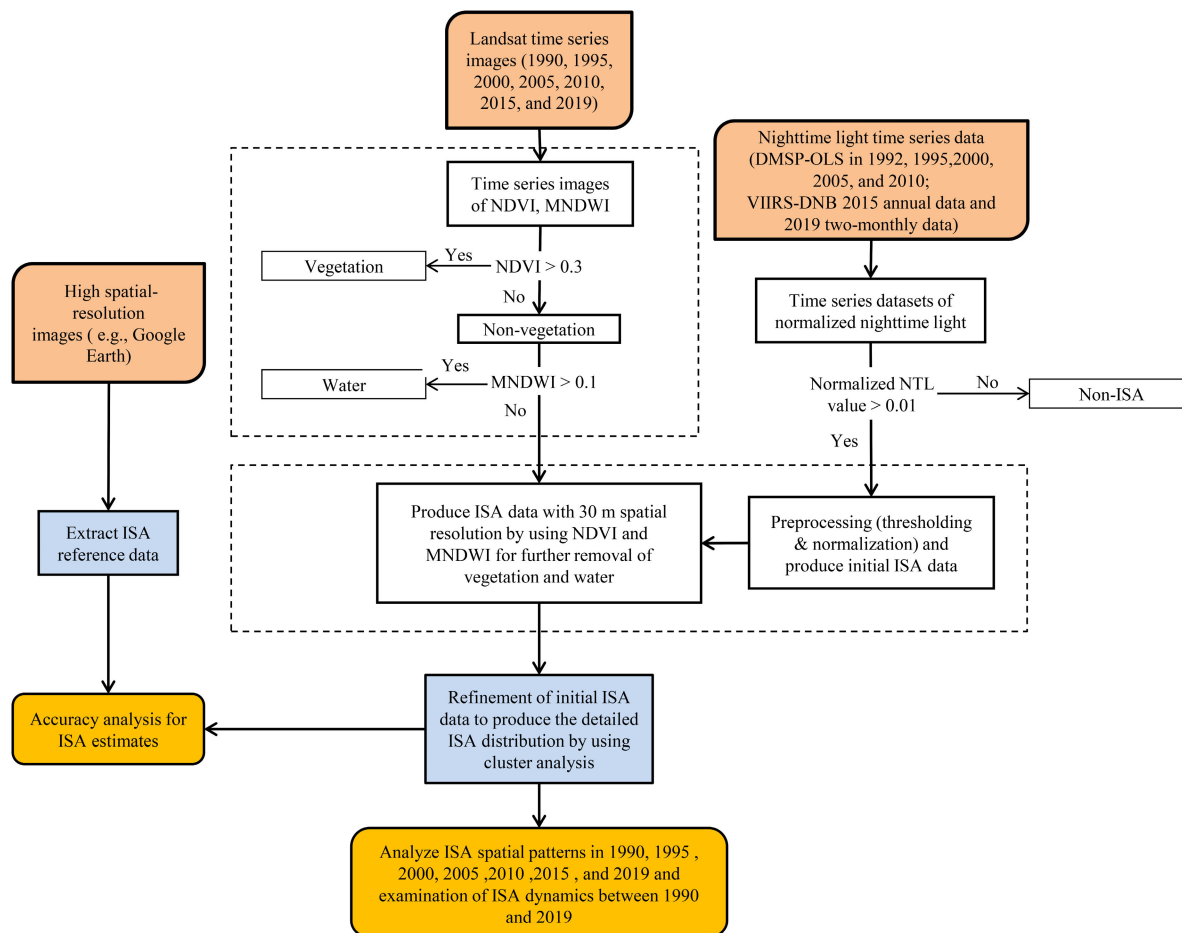
$$IISI = log_2(1 + \sqrt{DNB_{nor}}) \quad (4)$$

FIGURE 2. Framework for mapping the fractional ISA dynamics in Ordos.

where DNB_{nor} represents normalized VIIRS-DNB data which can obtained from (3). This logarithm model and coefficient can keep the value between 0 and 1.

3) USING THE THRESHOLD ALGORITHM TO EXTRACT THE INITIAL ISA DATA

Based on the findings in previous research on the ISA mapping, the NTL data (VIIRS-DNB & DMSP-OLS) contains moonlight, gas flares, fires, clouds and background noise. All these interfering factors should be excluded in urban ISA mapping [22], [47]. Guo *et al.* used a threshold of 0.01 on normalized VIIRS-DNB data to extract ISAs in arid and semi-arid regions and achieved good results [10]. Meanwhile, Xu *et al.*, Kuang *et al.*, and Zhou *et al.* removed the background noise in DMSP-OLS by applying the thresholding algorithm [3], [45], [55]. In this study, the value of 0.01 as the minimum threshold is used for extracting the initial ISA from normalized NTL imagery, which effectively ruled out non-ISA pixels (e.g., water, soil, vegetation, and desert).

B. REFINEMENT OF THE INITIAL ISA DATA USING LANDSAT IMAGES

Three types of Landsat images are used in this research. Landsat-TM imagery covers seven bands, including one thermal infrared band with 120 m spatial resolution and six reflective bands with 30 m spatial resolution [56]. Landsat-ETM+ imagery covers eight bands, including one thermal infrared band with 60 m spatial resolution, six reflective bands with 30 m spatial resolution, and one panchromatic band with 15 m spatial resolution [57]. Landsat-OLI imagery covers 11 bands, there are two thermal infrared bands with 100 m spatial resolution, eight reflective bands with 30 m spatial resolution, and the last one is panchromatic band with higher spatial resolution (15m) [22], [58]. Reflective bands with 30 m spatial resolution are mainly used in this research. The time-series Landsat (TM, ETM+, and OLI) data for 1990, 1995, 2000, 2005, 2010, 2015, and 2019 with 30 m spatial resolution are all re-projected into the ACEA projection from the Universal Transverse Mercator (UTC) coordinate system.

As illustrated in Figure 2, ISA data was extracted from Landsat imagery using threshold and cluster analysis. The major procedures include (1) calculating NDVI and MNDWI to remove vegetation and water, (2) extracting spectral information and performing cluster analysis, (3) merging all the clusters until the last two kinds (ISA and non-ISA) and conduct accuracy assessment for ISA.

The results of previous research indicate that NDVI is most frequently used to distinguish vegetation from non-vegetation, while MNDWI can separate water from non-water land cover [22]. In this study, threshold value of 0.3 is used on NDVI to separate the vegetation information (i.e., the pixel was considered as vegetation when its NDVI value is greater than 0.3). Accordingly, threshold value of 0.1 is used on MNDWI data to exclude water information (i.e., the pixel is considered as water with its MNDWI value greater than 0.1).

After removing the water and vegetation areas in the initially produced Landsat images, the rest of pixels are mainly bare soil and ISA. Then the ISODATA algorithm is used to classify the rest pixels. In this research, we set the clusters as 100. The clusters are finally merged into ISA and non-ISA according to their spectral characteristics and visual interpretation results in Google Earth high-resolution imagery [21], [22], [47].

C. ACCURACY ANALYSIS OF THE ISA ESTIMATES AND EXAMINATION OF THE ISA SPATIAL PATTERNS AND DYNAMICS

The ISAs for 2010, 2015, and 2019 were evaluated using reference data from high spatial resolution images in the Google Earth. A random sampling method was employed to select the validation samples. 1200 samples comprising 800 non-ISA and 400 ISA were selected for each year. Traditionally, an error matrix is used to evaluate classification accuracy [59]. From the error matrix, overall, producer, and user accuracy, as well as the kappa coefficient, are often selected to evaluate pixel-level classification accuracy [59], [60]. ISAs for 1990, 1995, 2000 and 2005 were not evaluated because of the lack of high spatial resolution images. However, it can be assumed as the ISA mapping accuracy was similar because of the robust ISA mapping procedure used in this research. Finally, examination of the ISAs in 1990, 1995, 2000, 2005, 2010, 2015, and 2019, as well as the spatial dynamics for 1990–2019 in Ordos was successfully conducted.

D. SPECTRAL INDICES

To determine the effectiveness of the method used in this paper for mapping ISA, several other spectral indices such as MNDWI, NDVI, SAVI, UI, NDBI, IBI, and IBUIopt were employed to conduct a comparative analysis. The MNDWI is a well-known index for rapid mapping the distribution of water bodies. The NDVI and SAVI are spectral indices for accurate mapping the distribution of vegetation areas. The UI, NDBI, IBI, and IBUIopt are indices for quick mapping the distribution of built-up areas. The formulas for the indices are as fellow:

$$MNDWI = \frac{\rho_{Green} - \rho_{Swir1}}{\rho_{Green} + \rho_{Swir1}} \tag{5}$$

$$NDVI = \frac{\rho_{Nir} - \rho_{Red}}{\rho_{Nir} + \rho_{Red}} \tag{6}$$

$$SAVI = \frac{(\rho_{Nir} - \rho_{Red}) * (1 + l)}{(\rho_{Nir} + \rho_{Red} + l)} \tag{7}$$

$$UI = \frac{\rho_{Swir2} - \rho_{Nir}}{\rho_{Swir2} + \rho_{Nir}} \tag{8}$$

$$NDBI = \frac{\rho_{Swir1} - \rho_{Nir}}{\rho_{Swir1} + \rho_{Nir}} \tag{9}$$

$$IBI = \frac{NDBI - (SAVI + MNDWI)\big/2}{NDBI + (SAVI + MNDWI)\big/2} \tag{10}$$

$$IBUI_{opt} = NDBI - SAVI - MNDWI \tag{11}$$

where ρ_{Green}, ρ_{Red}, ρ_{Nir}, ρ_{Swir1}, and ρ_{Swir2} are the surface reflectance values of the green, red, near-infrared, first shortwave infrared, and second shortwave infrared bands respectively. l is a constant whose value depends on the soil properties ($l = 0.5$ in this study).

TABLE 3. Accuracy assessment results of ISA estimates.

Years	Classified data	Reference data		PA	UA	OA	KC
		ISA	Non-ISA				
2010	ISA	349	51	84.9%	87.3%	90.6%	0.79
	Non-ISA	62	738	93.5%	92.3%		
2015	ISA	358	42	80.3%	89.5%	89.2%	0.76
	Non-ISA	88	712	94.4%	89.0%		
2019	ISA	373	27	84.0%	93.2%	91.8%	0.82
	Non-ISA	71	729	96.4%	91.1%		

Note: ISA, impervious surface area; PA, producer accuracy; UA, user accuracy; OA, overall accuracy; KC, kappa coefficient. Google Earth high spatial resolution images for 2010, 2015, and 2019 were used here as the corresponding year reference data.

IV. RESULTS
A. ACCURACY ASSESSMENT OF THE ISA ESTIMATES

The results of the accuracy assessment using these metrics for the ISA estimates are summarized in the Table 3. Using the validation samples for the corresponding years of 2010, 2015, and 2019, the ISAs are accurately extracted with overall accuracies of 90.6%, 89.2%, and 91.8% with kappa coefficients of 0.79, 0.76, and 0.82 respectively. The ISA mapping performance in 2019 is higher than those in 2010 and 2015 which were major reasons of the expansion of the ISA and sufficient high-resolution images for the classification. Compared to the ISA results in southern China, the accuracy in this study was slightly lower because of the similar spectral signatures of the ISA and bare soil [47]. Although accuracy assessments of the ISA results for 1990, 1995, 2000, and 2005 were not conducted, the visual interpretation of these results with corresponding Landsat images confirmed their accuracy.
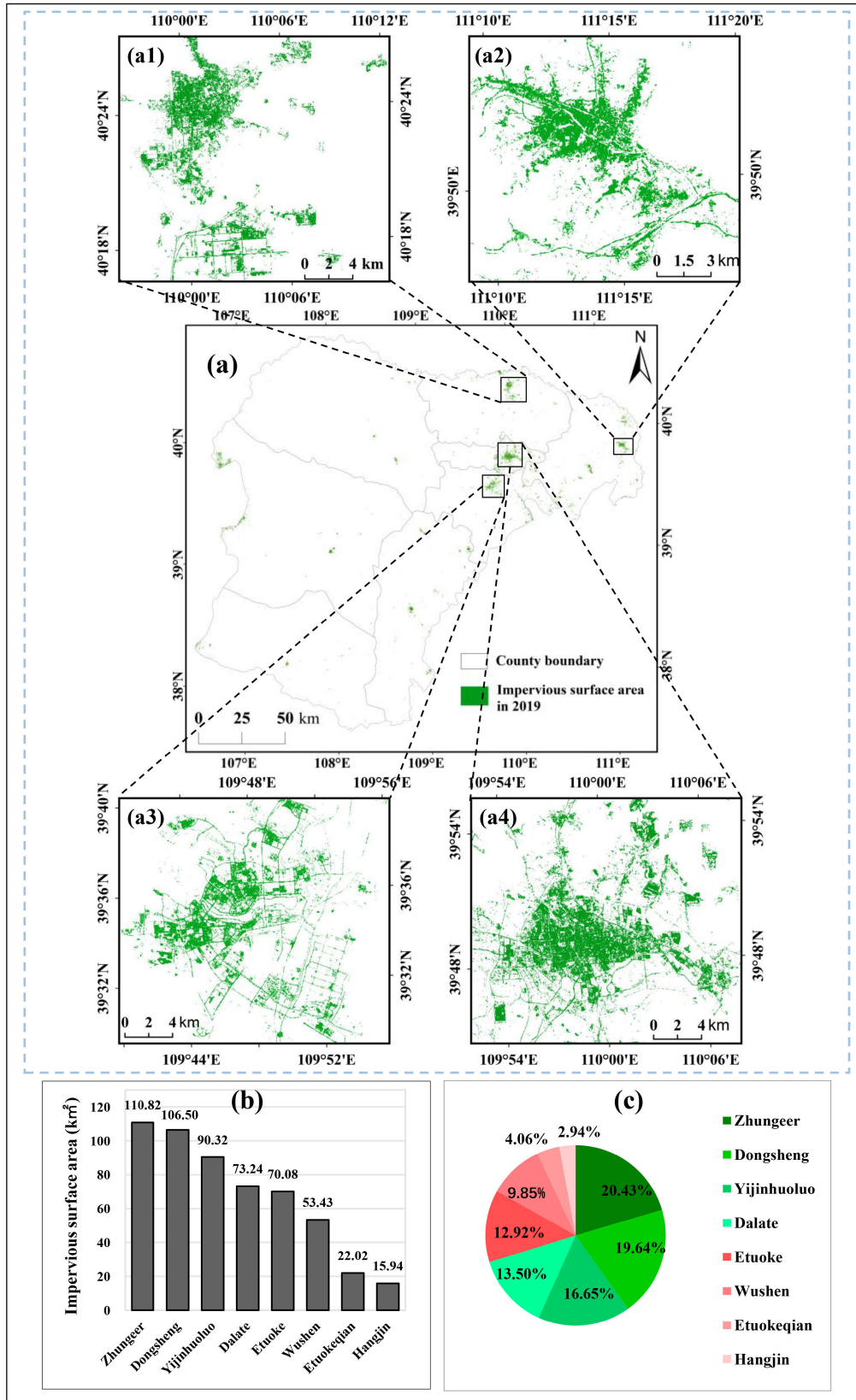
FIGURE 3. Spatial distribution of the ISA in the Ordos region in 2019. (a) ISA spatial distribution in Ordos ((a1) Dalate banner, (a2) Zhungeer banner, (a3) Yijinhuoluo banner, (a4) Dongsheng district) and (b) the size and (c) percentage of the ISA in each county in 2019.

B. EXAMINATION OF THE ISA SPATIAL PATTERNS AND DYNAMIC CHANGES

The ISA of Ordos is 529.71 km^2 in 2019, accounts for 0.61% of the entire area. We found that the ISA is mainly located in the north-eastern part of Ordos (380.7 km^2 accounting 70.22% of the total ISA) (Figure 3). The Zhungeer banner has the largest ISA of 110.8 km^2 (20.43% of the total ISA) followed by the Dongsheng district, the Yijinhuoluo banner, and the Dalate banner with 106.5, 90.3, and 73.2 km^2 (19.64%, 16.65%, and 13.50% of the total ISA), respectively. The highest ISA in Zhungeer Banner is related to the fact that the area is rich in coal resources. It has 23% of the city's population living in that areas, has a large number of industrial enterprises and the highest GDP of Ordos city. Likewise, Dongsheng District has significant mineral resources and was elected as one of the top 100 industrial counties in China in 2018 and 2019.

The south-western region of Ordos (Etuoke banner, Wushen banner, Etuokeqian banner, and Hangjin banner) accounted for 29.78% of the total ISA. The ISA in the Etuoke banner is 70.1 km^2 (12.92% of the total ISA), followed by Wushen banner, Etuokeqian banner, and Hangjin banner with 53.4, 22.0, and 15.9 km^2 (9.85%, 4.06%, and 2.94% of the total ISA), respectively.

The ISA in the Ordos region expanded rapidly from 1990–2019. As shown in Figure 4a, from 1990–2000, the ISA concentrated in a small area and tended to expand outwards (e.g., Dongsheng district and Yijinhuoluo banner). From 2000–2010, the ISA in Yijinhuoluo banner expanded to the northeast and the ISA in Dongsheng district expanded to the southwest. From 2010–2015, the ISA in the entire Ordos region expanded significantly. The ISA of the Zhungeer banner, the Dongsheng district, the Yijinhuoluo banner, and the Dalate banner expanded from the county center to the surrounding area due to large numbers of road networks and buildings built in the Dongsheng district and the Yijinhuoluo banner. For the period from 2015–2019, the ISA in the Zhungeer banner continued to extend in the surrounding area, while the ISA of the Dongsheng district and Dalate banner extended to the northeast. However, the ISA in Yijinhuoluo banner did not increase significantly.

The ISA increased 90.76 times from 5.76 km^2 to 529.71 km^2, showing exponential growth ($y = 2.5164e^{0.7625x}$) with R^2 of 0.9835 (Figure 4b). For 1990–1995, 1995–2000, and 2000–2005, the ISA increases in Ordos are less than 50 km^2 (8.70, 6.89, and 16.69 km^2, respectively). From 2005–2010, 2010–2015, and 2015–2019, the ISA increased substantially by 65.81 (1.73-fold), 217.72 (2.10-fold), and 208.14 km^2 (9.99-fold), respectively.

The Western Development Strategy was deployed in 2001 and accelerated in 2006. The ISA in Ordos increases tremendously from 2010-2019. During the period 2010-2015, the ISA increased the most in Ordos, mainly due to economic policies. GDP in Ordos increased by 158.29 billion yuan during this period with the best coal benefits and increased government investment in buildings and factories. A series of policies were implemented by the government to improve infrastructure conditions in 2010 such as the construction of the airport in Yijinhuoluo Banner (Figure 3a3 & Figure 4a3). The substantial increase in ISA in Ordos from 2015-2019 is related to the policy of the ''13th Five-Year Plan for Western Development'' implemented by the Inner Mongolia in 2017, which involves the construction of major railway and road transportation projects.

### C. COMPARATIVE ANALYSIS WITH OTHER INDICES

Taking the Dongsheng district and Yijinhuoluo banner as examples, the UI, NDBI, IBI, and IBUIopt images are obtained using the equations (5)-(11). Figure 5 shows extracted ISA using the five methods. As it can be seen, bare soil and arid land surfaces are the main interference sources of the five algorithms. Especially in arid and semi-arid areas using remote sensing data to map ISA accurately is difficult due to the complexity of large amounts of bare soil.

As shown in Figure 5, the UI algorithm can extract ISA using spectral information, but confounds a large amount of bare soil information in the results while not removing the water bodies effectively. The ISA extraction results of the NDBI algorithm confound the bare soil information but outperform the extraction results of the UI algorithm. In addition, the NDBI algorithm does not remove the water bodies and extraction of the built-up area requires a water body mask. The SAVI index can be applied to the IBI algorithm to make full use of the vegetation and soil information, masking some of the bare soil. The ISA extraction results of the IBI algorithm still have residual bare soil and water bodies, especially the high albedo impervious surface with low extraction accuracy. Compared to the UI, NDBI and IBI algorithm, the ISA extraction results of the IBUIopt algorithm have a higher accuracy, especially in densely built-up urban areas. However, the extraction results are still confused with wasteland and dry bare soil. None of the above four algorithms can extract roads effectively such as discontinuous roads and the roads are confused with the surrounding bare soil and vegetation. Comparative experiments in two regions show that the method in this paper can mask water bodies and vegetation effectively as well as removes a large amount of bare soil information. The extraction of ISA in arid and semi-arid areas is more effective when using the method in this paper than the other four methods mentioned above.

D. CORRELATION ANALYSIS BETWEEN THE ISA AND SOCIOECONOMIC FACTORS

From 1990–2019, the ISA of Ordos, a typical resource-based city, expanded significantly. In previous research, socioeconomic factors have often been used as the internal driving force for urban development [1]. In this research, we selected 15 socioeconomic factors including the national economy, population, income, and production and investment. We found that the ISA in the typical resource-based city of Ordos has strong correlations with socioeconomic factors (PGDP, LGR, and CP) from 1990–2019 (Figure 6).
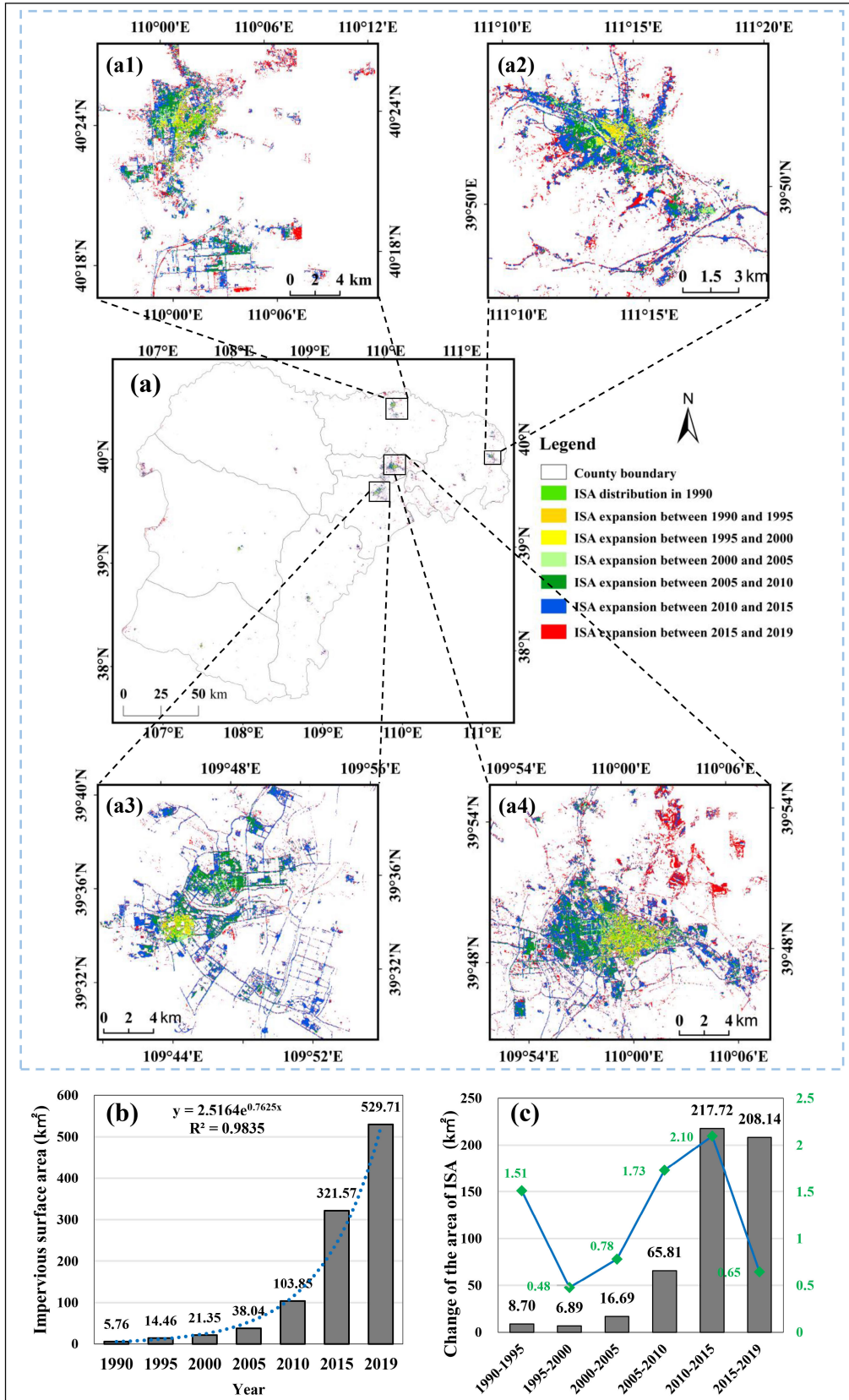
FIGURE 4. Spatial patterns of ISA expansion from 1990 to 2019 in the Ordos region. (a) ISA expansion in Ordos ((a1) Dalate banner, (a2) Zhungeer banner, (a3) Yijinhuoluo banner, and (a4) Dongsheng district) and ISA area (b) yearly increase from 1990 to 2019 and (c) five-yearly growth and growth rate.
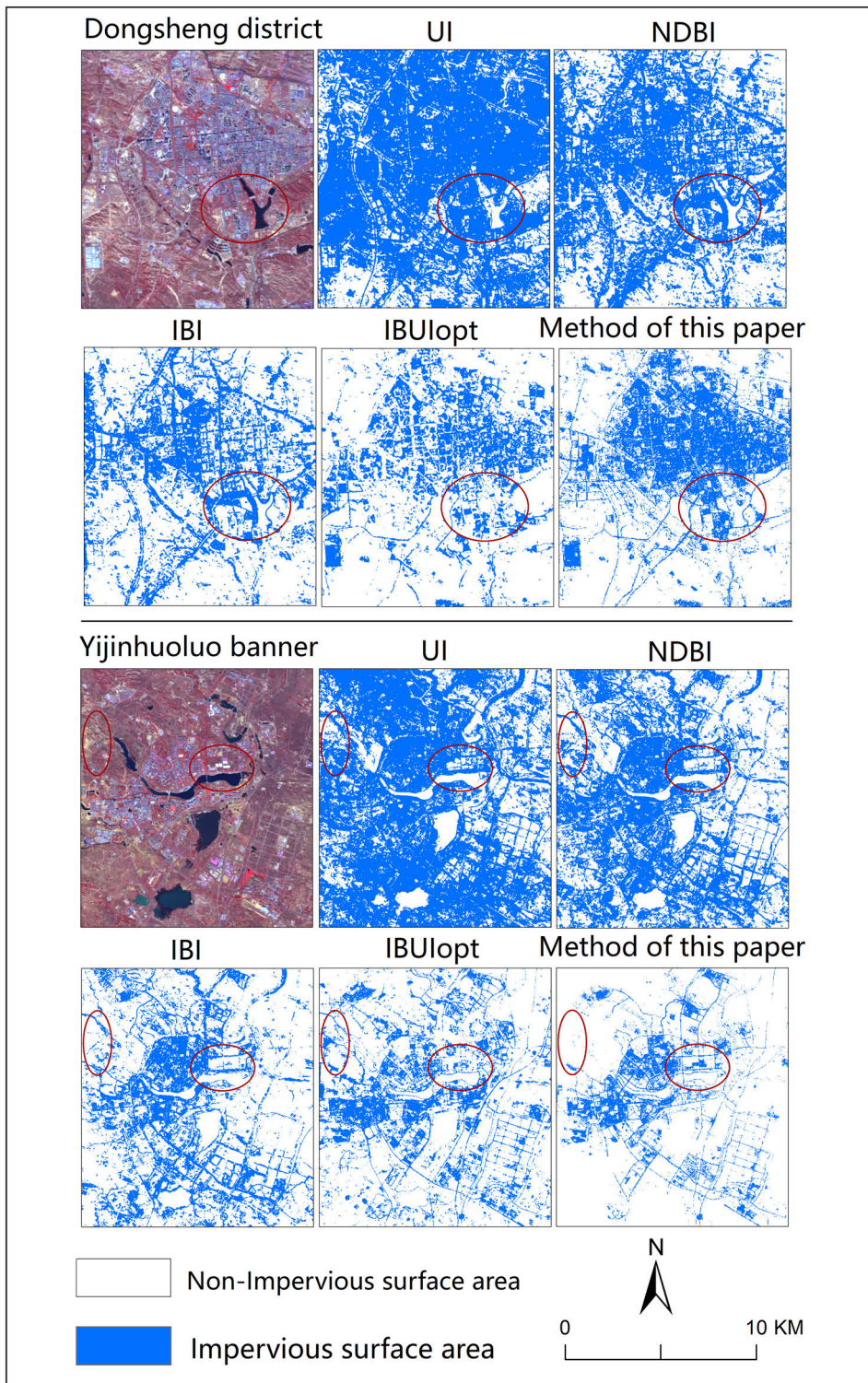
FIGURE 5. Extraction of Impervious surface area using each type of index/remote sensing data transformation.

The area of the ISA in the Ordos region has a positive correlation ($R > 0.92$) with the national economy at the significance level of 0.01 (Figure 6a). For the national economy, the area of ISA has positive correlations with TGDP ($R = 0.949$), GDPS ($R = 0.925$), GDPT ($R = 0.936$), and PGDP ($R = 0.942$). The ISA also has a positive correlation
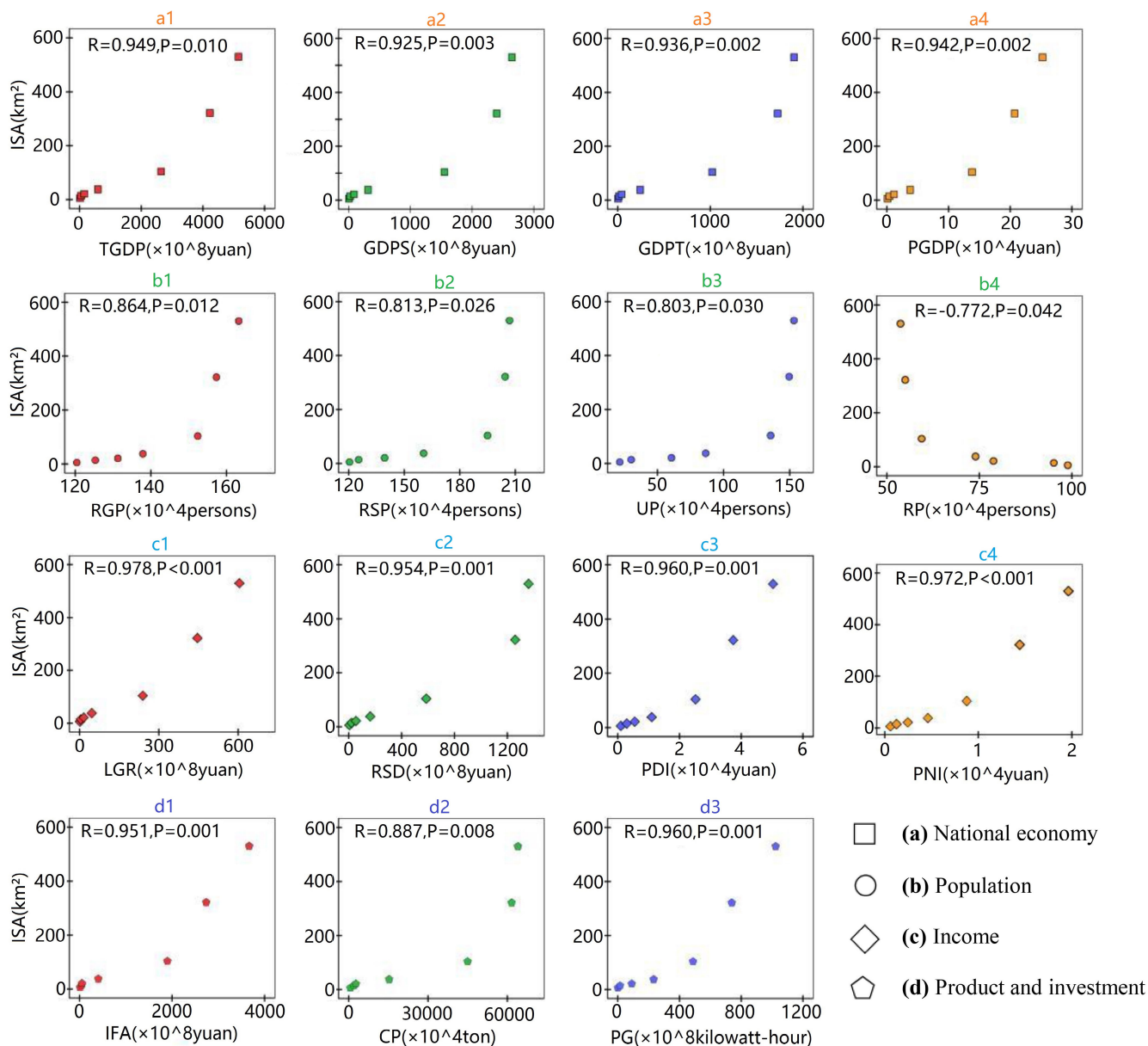
FIGURE 6. The relationships between the ISA and socioeconomic factors. (a) National economy, (b) population, (c) income, and (d) production and investment. GDP, gross domestic product.

($R > 0.950$) with income at the significance level of 0.01 (Figure 6c). It has positive correlations with LGR ($R = 0.978$), RSD ($R = 0.954$), PDI ($R = 0.960$), and PNI ($R = 0.972$). The ISA also has a positive correlation ($R > 0.88$) with IFA, CP, and PG at the significance level of 0.01 (Figure 6d). As shown in Figure 6b, the ISA has positive correlations ($R > 0.80$) with the RGP, RSP, and UP at the significance level of 0.05. In addition, it has a negative correlation ($R = -0.772$) with the RP at the significance level of 0.05.

Through the correlation analysis, we found that the ISA expansion was positively correlated with an increase in the national economy (e.g., GDP), income (e.g., LGR, PNI,

and PDI), production (e.g., PG), and investment (e.g., IFA). For the population factors, the ISA has expanded with the increases in the RGP, RSP, and UP. In other words, socioeconomic development of the Ordos region accelerated urban development and ISA expansion.

In addition, we found that the ISA of the typical resourcebased city of Ordos is more strongly correlated with economic factors than population factors. At the significance level of 0.05, the correlations between the ISA and the population factors are all less than 0.87 and the average correlation of the four population indicators is 0.813. However, at a significance level of 0.001, most of the economic indicators are greater than 0.92 (except for coal production) and
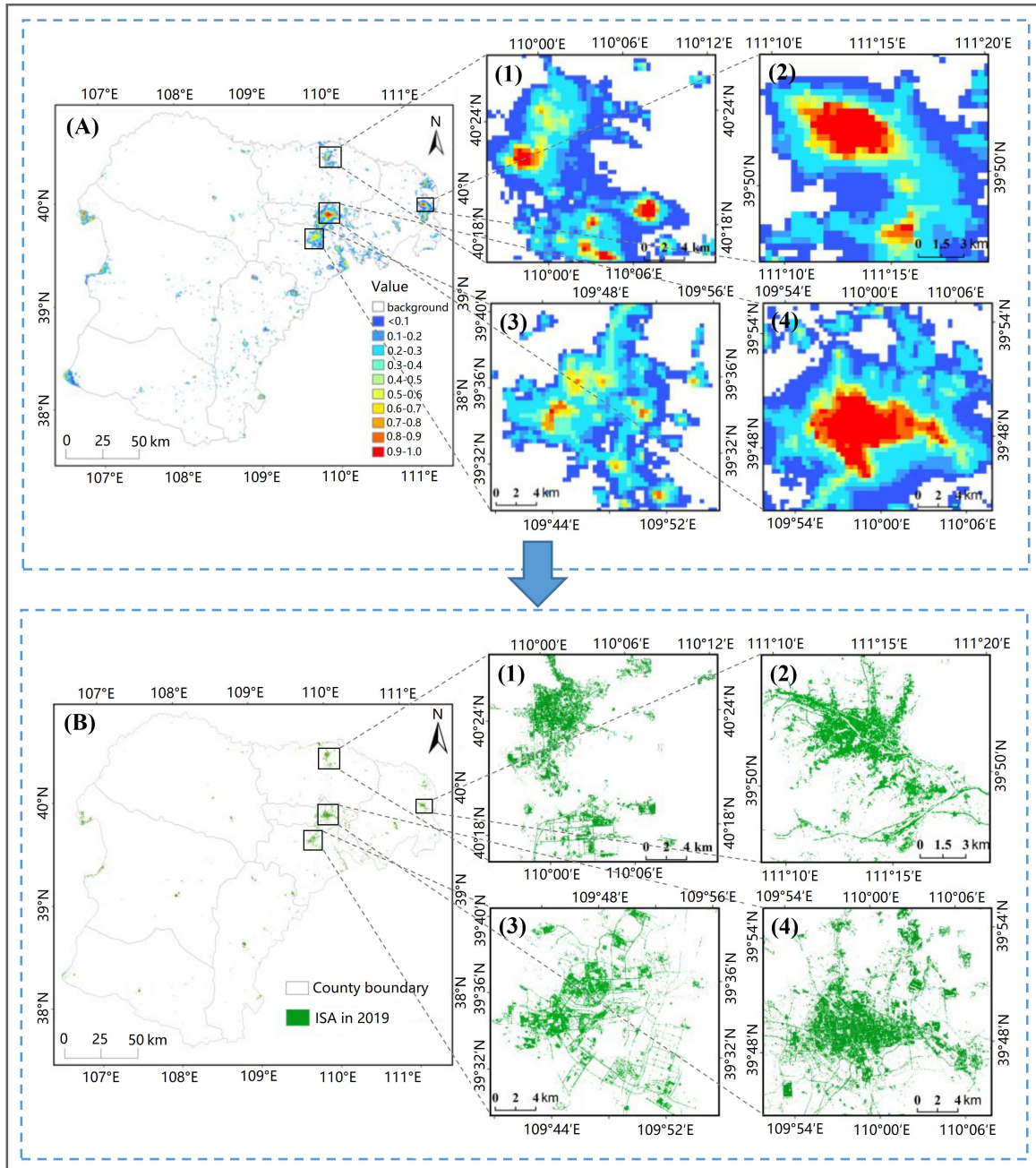
FIGURE 7. Comparison of the initial and refined ISA estimates for 2019. (A) NTL data and (B) Landsat imagery with 30 m spatial resolution. (1) Dalate banner, (2) Zhungeer banner, (3) Yijinhuoluo banner, and (4) Dongsheng district.

the average of these indicators is 0.946. The total GDP of Ordos in 1990 was only 1.49 billion yuan and it reached 515.33 billion yuan in 2019, an increase of 344.9 times. From 1990-2019, ISA grew from 5.8 km^2 to 529.7 km^2, an increase of 90.3 times. However, due to the large base of population, the rate of population growth is slow. From 1990-2019, the growth rate of RGP, RSP, and UP are 0.36, 0.73 and 6.12 times respectively. Although there was a huge increase in the urban population, the greatest growth occurred

between 2005-2010 when the urban population increased by almost half a million. Whereas, the rest of the period falling into the slow growth category. The rapid growth of the urban population during this period may also be related to the good coal benefits of 2005-2010 that increased the demand of a large number of jobs. In addition, socio-economic growth is reflected in the construction of factories, airports and roads directly, so that changes in ISA are more strongly correlated with economic factors than with population factors.

V. DISCUSSION

Multiple remote sensing data sources have been used in ISA mapping, such as high (e.g., IKONOS, GaoFen, and QuickBird), medium (e.g., Landsat), and coarse (e.g., Modis and NTL data) spatial resolution images [15], [21], [23]. At regional and the global scales, MODIS imagery with 250 m spatial resolution and NTL data (e.g., DMSP-OLS with 1 km spatial resolution and VIIRS-DNB with 500 m spatial resolution) have been used in ISA mapping [22], [47], although high spatial resolution images are better for distinguishing features and can be used instead [25]–[27]. However, this data acquisition comes at a high acquisition cost, high data processing workload, and the long-term sequence monitoring cannot be performed [30]. Whereas, Landsat images are collected for long-term sequence monitoring and are freely available.

Using only Landsat or NTL images makes the ISA mapping of arid and semi-arid areas inaccurate because of confusing the ISA with bare soil and coarse spatial resolution [15]. Therefore, we propose the combined use of NTL and Landsat data for the ISA mapping. This approach first takes advantage of the NTL data which can remove most of the non-ISA and focuses on the initial ISA in city areas, especially, in removing the soil and sand information from suburb aeras in arid/semiarid region. Moreover, Landsat imagery can effectively distinguish ISA from vegetation and water areas in the urban landscape. As shown in Figure 7, the approach used in this study is valuable for ISA mapping and dynamic analysis in arid/semiarid regions. Accurate ISA mapping makes subsequent socioeconomic correlation analysis scientific and reliable, especially for Ordos city which is located in semiarid region and rely on resources to flourish.

There is uncertainty when mapping ISAs due to the immaturity of the technology and limitations in the remote sensing data. In this study, the ISA mapping is achieved using a threshold method for the NTL data (DMSP-OLS and VIIRS-DNB) to obtain the range of the initial ISA and remove the noise from the suburb area such as soil and sand. The selection of the threshold value is very important, if it is too small, it may increase the workload of processing the Landsat images, and if it is too large, the effective ISA region will be reduced due to the loss of regions with low ISA density. In this research, considering that Ordos located in semiarid area, we referred to a previous study and selected a suitable threshold value to process the NTL data [15]. To refine the ISA, NDVI and MNDWI were used to eliminate vegetation and water areas in produced Landsat images by setting thresholds. However, due to various climatic conditions and biomes, unique NDVI and MNDWI thresholds are not suitable for the entire area. To obtain the ISA from Landsat accurately, further cluster analysis needs to be conducted. At present, little research has been conducted to accurately extract ISAs in arid/semi-arid regions, we encourage researchers to explore the integration of temperature data with multi-source remote sensing data to map ISAs.

VI. CONCLUSION

A combination of NTL data (DMSP-OLS and VIIRS-DNB) and Landsat imagery is proved to be effective for ISA mapping in arid and semiarid regions. The Ordos city in China is a resource-based city located in semiarid, the results indicate that the ISAs in 2010, 2015, and 2019 were extracted with overall accuracies of 90.6%, 89.2%, 91.8% and with kappa coefficients of 0.79, 0.76, and 0.82 respectively. The ISA in Ordos is mainly distributed in the northeast (70.22% in 2019), with the area in Zhungeer banner being the largest (110.8 km^2; 20.43% of the entire ISA), and only 29.78% was distributed in the southwest. From 2010–2015 and 2015–2019, the increase in the ISA in Ordos exceeded 200 km^2, of which the largest growth rate from 2010–2015 was 2.10-fold higher. Compared to the UI, NDBI, IBI and IBI algorithm, the ISA extraction results in arid and semiarid areas is more effective when using the method in this paper. The correlation between 15 socioeconomic factors and the ISA was greater than 0.8 at the significance level of 0.05. Based on our finding, it can be concluded that the correlation between the economy of this typical resource-based city and ISA development was greater than that with the population. This method can be used to quickly update ISA datasets for arid and semiarid regions. At the same time, the spatial patterns and dynamic change of the ISA data for Ordos city are of great significance where it can aid in understanding socioeconomic and environmental changes and also provides a reference for the ISA analysis of other resource-based cities located in arid/semiarid areas.

APPENDIX A

SPECIFIC INFORMATION ON THE LANDSAT DATA USED IN THIS STUDY

Landsat Path/Row	TM 1990	TM 1995	TM 2000	ETM+ 2005	TM 2010	OLI 2015	OLI 2019
126/032	1987-09-15	1995-07-03	2002-07-14	2005-09-08	2009-08-07	2015-08-13	2019-06-03
126/033	1990-08-22	1995-07-03	2002-07-14	2005-06-20	2009-06-11	2015-05-07	2019-06-03
127/032	1990-08-13	1996-08-29	2000-06-13	2005-06-11	2009-06-02	2015-07-03	2018-05-22
127/033	1989-09-11	1996-08-13	2001-05-31	2006-06-14	2009-06-02	2015-07-03	2018-05-22
128/032	1991-08-07	1996-09-05	2000-11-11	2005-06-02	2010-08-24	2015-07-30	2019-07-03
128/033	1991-09-15	1996-09-05	2000-11-11	2005-06-02	2010-09-11	2015-10-17	2018-06-14
128/034	1991-08-23	1995-08-18	1999-09-22	2005-06-02	2010-09-10	2015-07-28	2019-06-01
129/032	1989-08-24	1995-09-10	2000-06-11	2005-09-13	2009-08-29	2015-09-05	2019-08-27
129/033	1991-08-30	1995-09-10	1999-08-12	2006-09-16	2009-05-31	2015-09-05	2019-07-26

ACKNOWLEDGMENT

REFERENCES

[1] C. Yang, B. Yu, Z. Chen, W. Song, Y. Zhou, X. Li, and J. Wu, "A Spatial-Socioeconomic urban development status curve from NPP-VIIRS nighttime light data," *Remote Sens.*, vol. 11, no. 20, pp. 2398–2419, Oct. 2019.

[2] J. Li, C. Li, F. Zhu, C. Song, and J. Wu, "Spatiotemporal pattern of urbanization in Shanghai, China between 1989 and 2005," *Landscape Ecol.*, vol. 28, no. 8, pp. 1545–1565, Oct. 2013.

[3] P. Xu, P. Jin, Y. Yang, and Q. Wang, "Evaluating urbanization and spatial-temporal pattern using the DMSP/OLS nighttime light data: A case study in Zhejiang Province," *Math. Probl. Eng.*, vol. 2016, no. 16, pp. 1–8, Jan. 2016.

[4] B. Yu, S. Shu, H. Liu, W. Song, J. Wu, L. Wang, and Z. Chen, "Object-based spatial cluster analysis of urban landscape pattern using nighttime light satellite images: A case study of China," *Int. J. Geograph. Inf. Sci.*, vol. 28, no. 11, pp. 2328–2355, 2014.

[5] W. Chen, R. Zheng, S. Zhang, H. Zeng, T. Zuo, C. Xia, Z. Yang, and J. He, "Cancer incidence and mortality in China in 2013: An analysis based on urbanization level," *Chin. J. Cancer Res.*, vol. 29, no. 1, pp. 1–10, 2017.

[6] B. Chen, Z. Nie, Z. Chen, and B. Xu, "Quantitative estimation of 21st-century urban greenspace changes in Chinese populous cities," *Sci. Total Environ.*, vol. 609, no. 31, pp. 956–965, Dec. 2017.

[7] T. Chen, A. Sun, and R. Niu, "Effect of land cover fractions on changes in surface urban heat islands using Landsat time-series images," *Int. J. Environ. Res. Public Health.*, vol. 16, no. 6, p. 971, Mar. 2019.

[8] J. Wu, "Urban sustainability: An inevitable goal of landscape research," *Landscape Ecol.*, vol. 25, no. 1, pp. 1–4, Dec. 2009.

[9] Y. Zhang, D. Yang, X. Zhang, W. Dong, and X. Zhang, "Regional structure and spatial morphology characteristics of oasis urban agglomeration in arid area—A case of urban agglomeration in northern slope of Tianshan mountains, northwest China," *Chin. Geographical Sci.*, vol. 19, no. 4, pp. 341–348, Dec. 2009.

[10] W. Guo, Y. Zhang, and L. Gao, "Using VIIRS-DNB and Landsat data for impervious surface area mapping in an arid/semiarid region," *Remote Sens. Lett.*, vol. 9, no. 6, pp. 587–596, Jun. 2018.

[11] C. Zhang, D. Lu, X. Chen, Y. Zhang, B. Maisupova, and Y. Tao, "The spatiotemporal patterns of vegetation coverage and biomass of the temperate deserts in central asia and their relationships with climate controls," *Remote Sens. Environ.*, vol. 175, pp. 271–281, Mar. 2016.

[12] B. Wu, B. Yu, S. Yao, Q. Wu, Z. Chen, and J. Wu, "A surface network based method for studying urban hierarchies by night time light remote sensing data," *Int. J. Geogr. Inf. Sci.*, vol. 33, no. 7, pp. 1377–1398, Apr. 2019.

[13] L. Ma, J. Wu, J. Li, J. Peng, and H. Liu, "Evaluating saturation correction methods for DMSP/OLS nighttime light data: A case study from China's cities," *Remote Sens.*, vol. 6, no. 10, pp. 9853–9872, Oct. 2014.

[14] Q. Zheng, J. Deng, R. Jiang, K. Wang, X. Xue, Y. Lin, Z. Huang, Z. Shen, J. Li, A. R. Shahtahmassebi, "Monitoring and assessing 'ghost cities' in Northeast China from the view of nighttime light remote sensing data," *Habitat Int.*, vol. 70, no. 1, pp. 34–42, Oct. 2017.

[15] W. Guo, G. Li, W. Ni, Y. Zhang, and D. Lu, "Exploring improvement of impervious surface estimation at national scale through integration of nighttime light and proba-V data," *GISci. Remote Sens.*, vol. 55, no. 5, pp. 699–717, Feb. 2018.

[16] L. Tong, S. Hu, and A. E. Frazier, "Mixed accuracy of nighttime lights (NTL)-based urban land identification using thresholds: Evidence from a hierarchical analysis in Wuhan metropolis, China," *Appl. Geography*, vol. 98, pp. 201–214, Sep. 2018.

[17] C. Zeng, A. Zhang, L. Liu, and Y. Liu, "Administrative restructuring and land-use intensity—A spatial explicit perspective," *Land Use Policy*, vol. 67, pp. 190–199, Sep. 2017.

[18] V. Srinivasan, K. C. Seto, R. Emerson, and S. M. Gorelick, "The impact of urbanization on water vulnerability: A coupled human–environment system approach for Chennai, India," *Global Environ. Change*, vol. 23, no. 1, pp. 229–239, Feb. 2013.

[19] L. Li and D. Lu, "Mapping population density distribution at multiple scales in Zhejiang province using Landsat thematic mapper and census data," *Int. J. Remote Sens.*, vol. 37, no. 18, pp. 4243–4260, May 2016.

[20] C. L. Arnold and C. J. Gibbons, "Impervious surface coverage: The emergence of a key environmental indicator," *J. Amer. Planning Assoc.*, vol. 62, no. 2, pp. 243–258, Jun. 1996.

[21] D. Lu, G. Li, W. Kuang, and E. Moran, "Methods to extract impervious surface areas from satellite images," *Int. J. Digit. Earth*, vol. 7, no. 2, pp. 37–41, Feb. 2014.

[22] W. Guo, D. Lu, Y. Wu, and J. Zhang, "Mapping impervious surface distribution with integration of SNNP VIIRS-DNB and MODIS NDVI data," *Remote Sens.*, vol. 7, no. 9, pp. 12459–12477, Sep. 2015.

[23] Q. Weng, "Remote sensing of impervious surfaces in the urban areas: Requirements, methods, and trends," *Remote Sens. Environ.*, vol. 117, no. 8, pp. 34–49, Jun. 2012.

[24] S. Liu, Q. Shi, and L. Zhang, "Few-shot hyperspectral image classification with unknown classes using multitask deep learning," *IEEE Trans. Geosci. Remote Sens.*, early access, Sep. 4, 2020, doi: 10.1109/TGRS.2020.3018879.

[25] C. Gomez, M. Mangeas, M. Petit, C. Corbane, P. Hamon, S. Hamon, A. De Kochko, D. Le Pierres, V. Poncet, and M. Despinoy, "Use of high-resolution satellite imagery in an integrated model to predict the distribution of shade coffee tree hybrid zones," *Remote Sens. Environ.*, vol. 114, no. 11, pp. 2731–2744, Nov. 2010.

[26] Y. Wang and D. Lu, "Mapping Torreya grandis spatial distribution using high spatial resolution satellite imagery with the expert rules-based approach," *Remote Sens.*, vol. 9, no. 6, p. 564, Jun. 2017.

[27] S. Reis and K. Taşdemir, "Identification of hazelnut fields using spectral and Gabor textural features," *ISPRS J. Photogramm. Remote Sens.*, vol. 66, no. 5, pp. 652–661, Sep. 2011.

[28] Q. Shi, M. Liu, X. Liu, P. Liu, P. Zhang, J. Yang, and X. Li, "Domain adaption for fine-grained urban village extraction from satellite images," *IEEE Geosci. Remote Sens. Lett.*, vol. 17, no. 8, pp. 1430–1434, Aug. 2020.

[29] H. Guo, Q. Shi, B. Du, L. Zhang, D. Wang, and H. Ding, "Scene-driven multitask parallel attention network for building extraction in high-resolution remote sensing images," *IEEE Trans. Geosci. Remote Sens.*, pp. 1–20, Aug. 2020.

[30] Z. Xie, Y. Chen, D. Lu, G. Li, and E. Chen, "Classification of land cover, forest, and tree species classes with ZiYuan-3 multispectral and stereo data," *Remote Sens.*, vol. 11, no. 2, pp. 43–61, Dec. 2019.

[31] M. Kawamura, S. Jayamana, and Y. Tsujiko, "Relation between social and environmental conditions in Colombo Sri Lanka and the urban index estimated by satellite remote sensing data," *Int. Arch. Photogramm. Remote Sens.*, vol. 31, pp. 321–326, 1996.

[32] Y. Zha, J. Gao, and S. Ni, "Use of normalized difference built-up index in automatically mapping urban areas from TM imagery," *Int. J. Remote Sens.*, vol. 24, no. 3, pp. 583–594, Jan. 2003.

[33] H. Xu, "A new index for delineating built-up land features in satellite imagery," *Int. J. Remote Sens.*, vol. 29, no. 14, pp. 4269–4276, 2008.

[34] S. Sinha, A. Santra, and S. S. Mitra, "Semi-automated impervious feature extraction using built-up indices developed from space-borne optical and SAR remotely sensed sensors," *Adv. Space Res.*, vol. 66, no. 6, pp. 1372–1385, Sep. 2020.

[35] Q. Zheng, Q. Weng, and K. Wang, "Developing a new cross-sensor calibration model for DMSP-OLS and Suomi-NPP VIIRS night-light imageries," *ISPRS J. Photogramm.*, vol. 153, no. 8, pp. 36–47, Oct. 2019.

[36] J. Ou, X. Liu, P. Liu, and X. Liu, "Evaluation of luojia 1-01 nighttime light imagery for impervious surface detection: A comparison with NPP-VIIRS nighttime light data," *Int. J. Appl. Earth Observ. Geoinf.*, vol. 81, pp. 1–12, Sep. 2019.

[37] C. D. Elvidge, P. Cinzano, D. R. Pettit, J. Arvesen, P. Sutton, C. Small, R. Nemani, T. Longcore, C. Rich, J. Safran, J. Weeks, and S. Ebener, "The nightsat mission concept," *Int. J. Remote Sens.*, vol. 28, no. 12, pp. 2645–2670, Jun. 2007.

[38] B. Yu, K. Shi, Y. Hu, C. Huang, Z. Chen, and J. Wu, "Poverty evaluation using NPP-VIIRS nighttime light composite data at the county level in China," *IEEE J. Sel. Topics Appl. Earth Observ. Remote Sens.*, vol. 8, no. 3, pp. 1217–1229, Mar. 2015.

[39] H. Letu, M. Hara, H. Yagi, K. Naoki, G. Tana, F. Nishio, and O. Shuhei, "Estimating energy consumption from night-time DMPS/OLS imagery after correcting for saturation effects," *Int. J. Remote Sens.*, vol. 31, no. 16, pp. 4443–4458, Aug. 2010.

[40] X. Chen and W. D. Nordhaus, "Using luminosity data as a proxy for economic statistics," *Proc. Nat. Acad. Sci. USA*, vol. 108, no. 21, pp. 94–8589, May 2011.

[41] C. Small, F. Pozzi, and C. Elvidge, "Spatial analysis of global urban extent from DMSP-OLS night lights," *Remote Sens. Environ.*, vol. 96, nos. 3–4, pp. 277–291, Jun. 2005.

[42] C. D. Elvidge, P. C. Sutton, T. Ghosh, B. T. Tuttle, K. E. Baugh, B. Bhaduri, and E. Bright, "A global poverty map derived from satellite data," *Comput. Geosci.*, vol. 35, no. 8, pp. 1652–1660, Aug. 2009.

[43] H. Bagan, H. Borjigin, and Y. Yamagata, "Assessing nighttime lights for mapping the urban areas of 50 cities across the globe," *Environ. Planning B, Urban Analytics City Sci.*, vol. 46, no. 6, pp. 1097–1114, Jul. 2019.

[44] W. T. Lawrence, M. L. Imhoff, N. Kerle, and D. Stutzer, "Quantifying urban land use and impact on soils in egypt using diurnal satellite imagery of the Earth surface," *Int. J. Remote Sens.*, vol. 23, no. 19, pp. 3921–3937, Jan. 2002.

[45] Y. Zhou, S. J. Smith, C. D. Elvidge, K. Zhao, A. Thomson, and M. Imhoff, "A cluster-based method to map urban area from DMSP/OLS nightlights," *Remote Sens. Environ.*, vol. 147, pp. 173–185, May 2014.

[46] D. Lu, H. Tian, G. Zhou, and H. Ge, "Regional mapping of human settlements in southeastern China with multisensor remotely sensed data," *Remote Sens. Environ.*, vol. 112, no. 9, pp. 3668–3679, Sep. 2008, doi: 10.1016/j.rse.2008.05.009.

[47] W. Guo, D. Lu, and W. Kuang, "Improving fractional impervious surface mapping performance through combination of DMSP-OLS and MODIS NDVI data," *Remote Sens.*, vol. 9, no. 4, p. 375, 2017.

[48] X. Xue, Z. Yu, S. Zhu, Q. Zheng, M. Weston, K. Wang, M. Gan, and H. Xu, "Delineating urban boundaries using Landsat 8 multispectral data and VIIRS nighttime light data," *Remote Sens.*, vol. 10, no. 5, p. 799, May 2018.

[49] Q. Ma, C. He, and X. Fang, "A rapid method for quantifying landscape-scale vegetation disturbances by surface coal mining in arid and semiarid regions," *Landscape Ecol.*, vol. 33, no. 12, pp. 2061–2070, Oct. 2018.

[50] Y. Yue, M. Li, A.-X. Zhu, X. Ye, R. Mao, J. Wan, and J. Dong, "Land degradation monitoring in the ordos plateau of China using an expert knowledge and BP-ANN-based approach," *Sustainable*, vol. 8, no. 11, pp. 67–82, Aug. 2016.

[51] Q. Ma, Y. Long, X. Jia, H. Wang, and Y. Li, "Vegetation response to climatic variation and human activities on the ordos plateau from 2000 to 2016," *Environ. Earth Sci.*, vol. 78, no. 24, pp. 125–136, Dec. 2019.

[52] J. Li, S. Zhou, D. Fu, K. Chen, C. Zhang, Z. Sun, and P. Li, "Characteristics of desorption gas of lacustrine shale in the ordos basin, China," *IOP Conf. Earth Environ. Sci.*, vol. 360, no. 2, pp. 32–45, Dec. 2019.

[53] C. D. Elvidge, J. Safran, B. Tuttle, P. Sutton, P. Cinzano, D. Pettit, J. Arvesen, and C. Small, "Potential for global mapping of development via a nightsat mission," *GeoJournal*, vol. 69, nos. 1–2, pp. 45–53, 2007.

[54] J. Wu, S. He, J. Peng, W. Li, and X. Zhong, "Intercalibration of DMSP-OLS night-time light data by the invariant region method," *Int. J. Remote Sens.*, vol. 34, no. 20, pp. 7356–7368, Oct. 2013.

[55] W. Kuang, J. Liu, Z. Zhang, D. Lu, and B. Xiang, "Spatiotemporal dynamics of impervious surface areas across China during the early 21st century," *Chin. Sci. Bull.*, vol. 58, no. 14, pp. 1691–1701, May 2013.

[56] B. Haack, N. Bryant, and S. Adams, "An assessment of Landsat MSS and TM data for urban and near-urban land-cover digital classification," *Remote Sens. Environ.*, vol. 21, no. 2, pp. 201–213, Mar. 1987.

[57] L. Eklundh, L. Harrie, and A. Kuusk, "Investigating relationships between Landsat ETM+ sensor data and leaf area index in a boreal conifer forest," *Remote Sens. Environ.*, vol. 12, no. 8, pp. 239–251, May 2001.

[58] B. Kumari, M. Tayyab, J. Mallick, M. F. Khan, and A. Rahman, "Satellite-driven land surface temperature (LST) using Landsat 5, 7 (TM/ETM+ SLC) and Landsat 8 (OLI/TIRS) data and its association with built-up and green cover over urban Delhi, India," *Remote Sens. Earth Syst. Sci.*, vol. 1, nos. 3–4, pp. 63–78, Feb. 2018.

[59] P. Hao, L. Wang, Y. Zhan, and Z. Niu, "Using moderate-resolution temporal NDVI profiles for high-resolution crop mapping in years of absent ground reference data: A case study of Bole and Manas Counties in Xinjiang, China," *ISPRS Int. J. Geo-Inf.*, vol. 5, no. 5, pp. 72–89, Apr. 2016.

[60] R. G. Congalton, "A review of assessing the accuracy of classifications of remotely sensed data," *Remote Sens. Environ.*, vol. 37, no. 1, pp. 35–46, 1991.

WEI GUO received the B.Eng. and M.Eng. degrees from the Shandong University of Science and Technology, Qingdao, China, in 2008 and 2011, respectively, and the Ph.D. degree in cartography and geographic information system from Wuhan University, Wuhan, China, in 2015.

He was a Visiting Scholar with Michigan State University from 2013 to 2015, and worked with the State Key Laboratory of Remote Sensing Science, Chinese Academy of Sciences, China, from 2016 to 2019. He is currently a Senior Lecturer with the College of Geoscience and Surveying Engineering, China University of Mining and Technology, Beijing, China. His research interests include urban remote sensing and ecological environment monitoring.

CHUANWU ZHAO was born in Xinyang, Henan, China, in 1995. He is currently pursuing the master's degree with the School of College of Geoscience and Surveying Engineering, China University of Mining and Technology, Beijing, China. His research interests include landscape ecology, urban remote sensing, and regional development.

YUHUAN ZHANG received the Ph.D. degree in cartography and geographic information system from the Chinese Academy of Sciences University, Beijing, China, in 2014.

She is currently a Senior Engineer with the Ministry of Ecology and Environment Center for Satellite Application on Ecology and Environment. Her scientific interests include aerosol retrieval, in-flight calibration for remote sensing satellite sensors, and atmospheric remote sensing.

SHANGQING GAO was born in Jiaozuo, Henan, China, in 1995. She is currently pursuing the Ph.D. degree with the School of Graduate School of Education, Beijing Foreign Studies University, Beijing, China. Her research interests include foreign language and literature, translation, international education, and sociology.

• • •